



Wall length-based deformation monitoring method of brick-concrete buildings in mining area using terrestrial laser scanning

Jingyu Li^{1,2} · Lei Wang² · Jinzhong Huang²

Received: 27 November 2022 / Accepted: 9 April 2023 / Published online: 15 April 2023
© Springer-Verlag GmbH Germany, part of Springer Nature 2023

Abstract

For brick-concrete buildings which are easily damaged by mining activities, this study conducted measurements using a terrestrial laser scanning and adopted the wall length as a deformation monitoring index. First, the point cloud data of the individual walls are extracted by segmenting the building-point cloud data and redistributing the wall-point cloud data. Second, after individual walls were rotated, the boundary points of all the wall-point clouds were estimated. Third, based on boundary points, the top boundary lines are fitted using the weighted iterative least squares method by applying the constraint that two adjacent (top) boundary lines intersect at a common point. Fourth, multiple regions of interest were constructed by performing downward translations on each wall, and the length of the wall was calculated at these regions. Finally, for a brick-concrete building in the coal mining area, the difference between the wall lengths of two consecutive measurements at the same interest-region was estimated to obtain the deformation information about the building. The results show that the deformation estimated using the proposed method is consistent with the actual deformation of the building as reflected by the wall fractures. The method exhibits millimeter-level accuracy in determining the wall length, with an absolute error in the range – 6 to 6 mm.

Keywords Terrestrial laser scanning · Brick-concrete building · Deformation monitoring · Mining disaster · Point clouds

1 Introduction

Rural areas are the main mining areas of mineral resources in China, and the low brick-concrete buildings are the primary components of buildings in rural areas. Such brick-concrete buildings have a simple design. They do not possess any accessory structures, except for doors and windows, and are relatively low-cost [1]. However, such buildings are easily affected by the movement of the surface rock strata, especially which caused by frequent mining activities [2, 3]. Therefore, it is crucial to monitor the deformation of such buildings to assess the extent of their structural damage.

Traditionally, total stations are used for the deformation monitoring of brick-concrete buildings. However, only a few

discrete points can be measured using a total station, making it a time-consuming and laborious process. New monitoring methods based on differential interferometric synthetic aperture radar (DInSAR), unmanned aerial vehicle (UAV) photogrammetry, and terrestrial laser scanning (TLS) have gradually emerged with the advancement of surveying and mapping technology [4–6]. Currently, TLS is the most widely used technique because it represents object surface information in the form of massive high-precision point clouds, unlike DInSAR and UAV photogrammetry [7, 8].

Building deformation monitoring using TLS can be divided into two categories: (1) monitoring using established models and (2) monitoring using customized indices. Examples of category (1) include the study by Nieto-Julián et al., who proposed a building information model (BIM) to calculate the change in displacement of a building between two measurements [9]. In addition, Rolin et al. proposed a BIM to determine the change in displacement and stress of a building under applied gravity [10]. Moreover, Lian et al. used a finite element model to estimate the change in wall principal stress and shear stress of a building under mining conditions [11]. Examples of category (2) include the study by Batur et al., who considered the displacement of a

✉ Lei Wang
austwlei@163.com

¹ College of Geoscience and Surveying Engineering, China University of Mining and Technology-Beijing, Beijing 100083, China

² School of Spatial Information and Geomatics Engineering, Anhui University of Science and Technology, Huainan 232001, China

building as a monitoring index and used the cloud-to-cloud method to register and filter the point cloud data for deformation monitoring [12]. Li et al. considered wall subsidence cracks and horizontal displacement as indices for conducting deformation monitoring in combination with a subsidence prediction model [13]. Furthermore, Yang et al. considered wall inclination and crack depth as deformation monitoring indices in combination with a triangular mesh vector model developed using the alpha shape algorithm [14]. Thus, compared to established models, customized indices provide more flexibility for monitoring the deformation of buildings under different scenarios.

Subsidence, inclination, curvature, horizontal displacement, and horizontal deformation are the most common indices used for monitoring deformation of brick-concrete building in Chinese mining areas [15, 16]. Subsidence and horizontal displacement are primarily caused by a change in the groundwater level and do not cause major structural damage to the buildings. In practice, other three deformations is typically measured by placing artificial signs on buildings, especially those found in coal-mining regions. However, this work need to be registered for the same coordinates [17, 18]. This requires considerable manpower and material resources and also introduces a lot of errors. When the structural damage caused by above three deformations reaches a certain level, cracks appear on the walls, which in turn changes the length of the walls. Therefore, this study conducted measurements of brick-concrete buildings using a terrestrial laser scanning and adopted the wall length as a deformation monitoring index, which, can measure the change in the length of the building walls due to the deformation caused by mining activities.

The remainder of this paper is organized as follows. Section 2 introduces the basic principles and methods used in this study. Section 3 presents a case study, including: an overview; details of the monitoring process; the method for determining the thickness of the wall-point clouds; and the results of the wall length calculations and corresponding deformation analysis. Section 4 compares different boundary point estimation methods, discusses the effect of different weight functions on the wall length, and evaluates the accuracy of the proposed method. Finally, Sect. 5 summarizes the conclusions of this study.

2 Methodology

2.1 Basic principles

In this study, the random sample consensus (RANSAC) and weighted iterative least squares (WILS) algorithms were used to calculate the length of the building walls [19, 20].

2.1.1 RANSAC algorithm

When a given dataset can be clearly described by a specific model and contains no significant errors or outliers, then the least squares (LS) method can be used to determine the model parameters using the following equation [21]:

$$X = (B^T P B)^{-1} B^T P L \quad (1)$$

where X is the matrix of model parameters, B is the coefficient matrix, L is the matrix of measured values, and P is the weight matrix for the measured values ($P_{ij} = 0$ if $i \neq j$). Note that in the absence of any errors or outliers, P is a unit matrix.

In reality, the complete absence of outliers in a dataset cannot be guaranteed; moreover, it is difficult to separate the outliers from the relevant data or “inliers” effectively. For a given dataset that can be fitted using a model, RANSAC solves this problem of data separation as follows.

- (1) n data points are randomly selected from the dataset and Eq. (1) is used to solve for the model parameters.
- (2) The geometric distance between the data point and estimated model is calculated and only those data points whose distance is less than the distance threshold are retained.
- (3) The above two steps are iteratively repeated. After a fixed number of iterations, the data points that fit the model well are considered to be the inliers.

In addition, the RANSAC algorithm estimates the parameters of the best fit model. The final model is considered to be the one corresponding to the maximum number of inliers.

2.1.2 WILS method

The presence of outliers in the dataset affects both the LS and RANSAC algorithms. This is mitigated by the WILS method, which adjusts the weights of the outliers using an appropriate weight function.

Considering the IGG weight function (given by Eq. (3)) as an example, the WILS algorithm solves for the model parameters as follows [22].

- (1) The model parameters for a given dataset are obtained using Eq. (1).
- (2) The residual value for each measurement is calculated using Eq. (2). The weight matrix of the measured values is then updated according to Eq. (3).
- (3) The above two steps are iteratively repeated. The parameters of the best fit model are obtained after a fixed number of iterations.

$$V = BX - L, \tag{2}$$

where V is the residual matrix for each measurement and

$$p_{ii} = \begin{cases} 1 & |v_i| < s_1\sigma_0 \\ s_1\sigma_0/|v_i| & s_1\sigma_0 < |v_i| < s_2\sigma_0 \\ 0 & |v_i| > s_2\sigma_0 \end{cases} \tag{3}$$

where v_i is the residual of the i -th measurement; s_1 and s_2 are the threshold coefficients to ensure robustness; and σ_0 is the standard deviation of the residual. In this study, s_1 and s_2 were taken to be 1.0 and 2.5, respectively.

2.2 Acquisition of individual wall-point cloud data

Walls are the basic units of a building, and the objective of the present study is to calculate the length of a wall under deformation. However, in addition to the point clouds representing the walls of the building, the TLS obtains point clouds representing other objects in its scanning field. Therefore, the point cloud data of the building consists of overlapping point clouds corresponding to the walls. In this section, we discuss the steps associated with the point cloud data acquisition.

2.2.1 Segmentation of building-point cloud data

Let us consider a building composed of four walls that are perpendicular to the XOY plane, as shown in Fig. 1. In this figure, single wall is represented by a straight line in the XOY plane, and the building is represented by the intersection of multiple straight lines in 3D space. In this study, we employed RANSAC for segmenting the 3D point cloud data.

First, the 3D point cloud data of the building was projected onto the XOY plane to decompose the data into four wall units. Next, RANSAC was used to determine the model corresponding to the maximum number of inlier points

representing the point cloud of single wall. Subsequently, the dataset was updated by deleting the point cloud data of this wall from that of the entire building. These steps were repeated until the point cloud data corresponding to all four walls were extracted.

The corresponding B , X , and L matrices are shown in Fig. 1. Note that to prevent the straight lines representing the four walls from overlapping on the XOY plane, the distance threshold should be greater than the thickness of the wall-point cloud. The method for determining the point cloud thickness is described in Sect. 3.2.

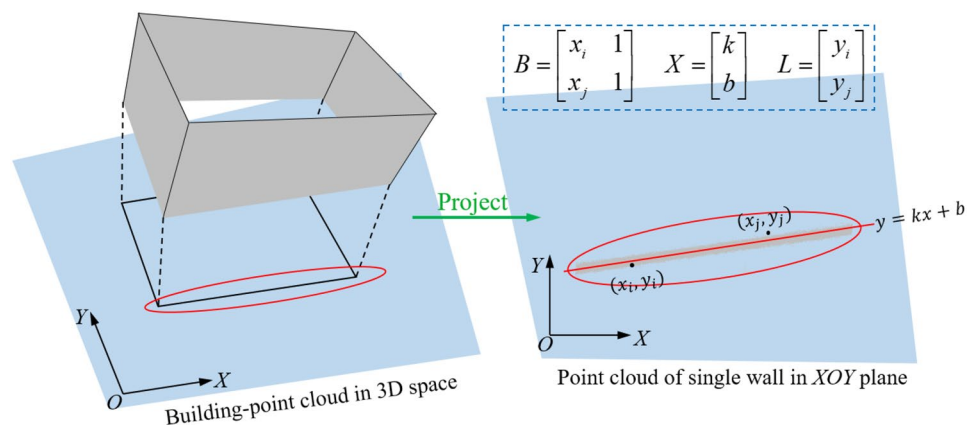
2.2.2 Redistribution of composite wall-point cloud data

Although considering a distance threshold greater than the point cloud thickness of the walls prevents the straight lines from overlapping on the XOY plane, it leads to over-segmentation of the 3D point cloud data.

Over-segmentation leads to the following issues: (1) the composite point cloud of the first wall extracted using RANSAC also includes the data points corresponding to the two adjacent walls; (2) the composite point cloud of the last wall extracted using RANSAC does not include the data points corresponding to the two adjacent walls; and (3) the composite point clouds of the second and third walls extracted using RANSAC include the data points corresponding to one adjacent wall but not the other. Therefore, the data points of the composite point clouds of all four walls need to be redistributed following the segmentation of the building-point cloud, as described below.

First, the true point cloud of a wall was extracted from its composite point cloud using RANSAC. Next, the difference between the composite point cloud and true point cloud of this wall was obtained. Subsequently, the distance from each data point of this wall to all other walls was determined. Finally, if this distance was less than the distance threshold, then the data point was assigned to the point cloud of the concerned wall.

Fig. 1 Point clouds corresponding to a building in 3D space and single wall in 2D plane



The corresponding B , X , and L matrices are shown in Fig. 2. Note that in this case, the distance threshold needs to be equal to the thickness of the wall-point cloud so that the same data point can be assigned to multiple walls.

2.3 Estimation of boundary points

The boundary points of a point cloud are generally estimated using normal vectors [23]. Let us consider a 3D coordinate system to describe a point cloud consisting of a point P_i and its neighbors. The boundary and non-boundary points in the XOY plane of the coordinate system are determined with respect to the point P_i . This method considers two types of neighborhoods for each point, which are used to calculate the normal and transformed coordinates of the data points, and consequently, estimate the boundary points of the cloud. The larger the neighborhood, more accurate is the boundary estimation; however, longer is the estimation time.

In a 3D coordinate system, when the parameters describing two planes are known, one plane can be rotated to become parallel to the other. Assuming X_A and X_B to be the model parameters of planes A and B , respectively, then the angle of rotation θ is given by

$$\theta = \text{Arccos}(X_A X_B / |X_A| |X_B|) \tag{4}$$

where $||$ denotes the modulus of the model parameters.

In this study, we assumed that all the data points of a point cloud representing a single wall lie approximately in the same plane. Moreover, we modified the above boundary point estimation method to improve the estimation time, namely, the boundary points were estimated after

rotating the wall-point cloud such that it was parallel to the XOY plane. The rotation process can be divided into two steps (see Eq. (5)):

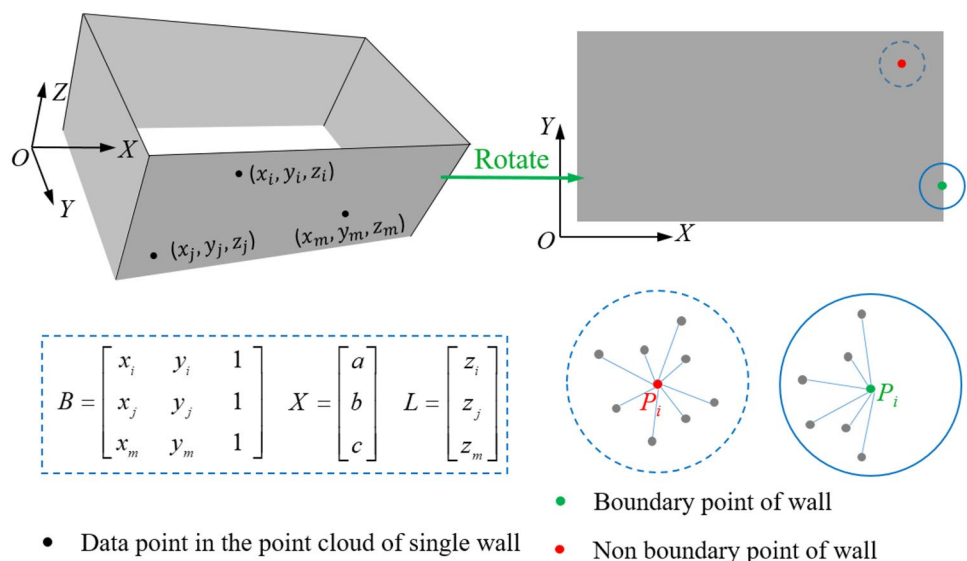
- (1) The wall-point cloud about the Z -axis was rotated such that it was parallel to the XOZ plane.
- (2) The wall-point cloud about the X -axis was rotated such that it was parallel to the XOY plane.

$$\begin{bmatrix} x' \\ y' \\ z' \end{bmatrix} = \begin{bmatrix} 1 & 0 & 0 \\ 0 & \cos \theta_2 & -\sin \theta_2 \\ 0 & \sin \theta_2 & \cos \theta_2 \end{bmatrix} \begin{bmatrix} \cos \theta_1 & -\sin \theta_1 & 0 \\ \sin \theta_1 & \cos \theta_1 & 0 \\ 0 & 0 & 1 \end{bmatrix} \begin{bmatrix} x \\ y \\ z \end{bmatrix} \tag{5}$$

where (x, y, z) and (x', y', z') are the coordinates before and after rotation, respectively; and θ_1 and θ_2 are the angles of rotation corresponding to steps (1) and (2), respectively.

The boundary point estimation method used in this study can be described as follows. First, the WLS method was used to solve for the model parameters of the planes. Next, the angle between the point cloud of a single wall and the XOY plane was calculated. The point cloud was then rotated such that it was parallel to the XOY plane, as described by Eq. (5). Figure 2 shows how the data point P_i is connected to its neighboring points in the new coordinate system. Subsequently, the angles between the adjacent connecting lines were calculated. Next, the difference between adjacent angles was calculated. If this difference was greater than the angle threshold, then point P_i was considered to be a boundary point. Finally, the inverse transformation of Eq. (5) was performed to return the boundary point to its original position prior to the rotation.

Fig. 2 Estimation of the boundary points of single wall



2.4 Fitting of top boundary line

The boundary points of a wall can be of two types: inner and outer. Inner boundary points arise due to the presence of doors, windows, or point cloud cavities and were ignored in our calculations. A boundary line is a straight line connecting the outer boundary points, which are again of two types: vertical and horizontal. In this study, we focused on the horizontal boundary lines along the roof, namely, the top boundary lines.

Note that the top boundary lines connecting two adjacent walls have a common intersection point, as shown in Fig. 3. The aforementioned boundary point estimation method is likely to introduce significant errors, which tend to negatively affect the LS and RANSAC methods. Therefore, the WILS method was used to find the best-fit model for the top boundary lines by imposing the constraint of intersection points, as outlined below.

First, a top boundary line was projected onto the *XOY* plane, and the WILS method was used to solve for the model parameters of the line. The corresponding *B*, *X* and *L* matrices are shown in Fig. 3. The angles between the plane containing the top boundary line and the *XOZ* and *YOZ* planes were calculated using Eq. (4). Next, the top boundary line was projected onto either the *XOZ* or *YOZ* plane at a smaller angle, and the model parameters of the line was again determined using the WILS method. The corresponding *B*, *X*, and *L* matrices are shown in Fig. 3. The top boundary lines *A* and *B* and their intersection points can be described by Eqs. (6) and (7), respectively. All the top boundary lines obey the following constraint: two adjacent boundary lines intersect at a point. If points (x_a, y_a, z_a) and (x_b, y_b, z_b) represent the two intersection points of line *A*, then line *A* can be fitted by Eq. (8).

$$k_1x + b_1 = y = (z - b_2)/k_2 \tag{6}$$

$$k_3x + b_3 = y = (z - b_4)/k_4 \tag{7}$$

$$\begin{aligned} \frac{x-f}{g} &= \frac{x-x_a + (x_a-x_b)/(y_a-y_b)y_a}{(x_a-x_b)/(y_a-y_b)} = y \\ &= \frac{z-z_a + (z_a-z_b)/(y_a-y_b)y_a}{(z_a-z_b)/(y_a-y_b)} = \frac{z-h}{l} \end{aligned} \tag{8}$$

2.5 Calculation of wall length

To calculate the length of a wall, the corresponding top boundary line was first translated downward by a step size of *H*, and a interest-region of height *2H* was defined about the translated boundary line.

The vertical boundary points are intercepted by the interest-region, as shown in Fig. 4. Because the boundary point estimation was performed on a single wall, the boundary

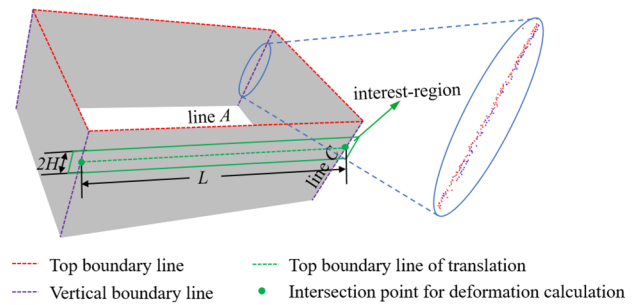
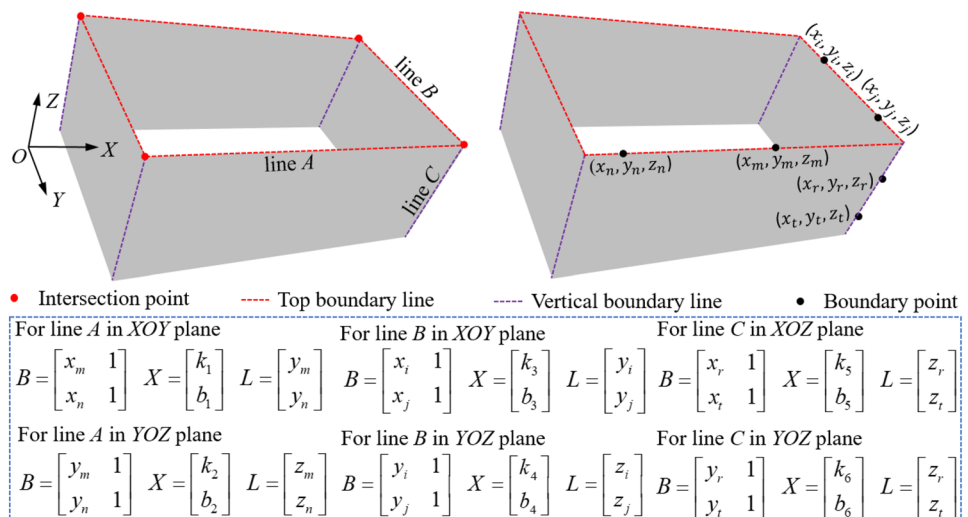


Fig. 4 Calculation of wall length at a interest-region

Fig. 3 Model parameters for the projected top boundary lines



points along a vertical boundary line were divided into two groups: those located on the same wall and those located on the adjacent wall. Therefore, first, the vertical boundary points were merged into one group; subsequently, the WILS method was used to determine the model parameters of the vertical boundary line in the interest-region. The corresponding B , X and L matrices are shown in Fig. 3. The vertical boundary line can be described by Eq. (9). The top boundary line A after the i -th translation can be described by Eq. (10). Assuming that points (x_a, y_a, z_a) and (x_b, y_b, z_b) are the two intersection points in the interest-region, the length of the wall can be calculated using Eq. (11).

$$k_5x + b_5 = k_6y + b_6 = z \quad (9)$$

$$(x - f)/g = y = (x - h - HI)/l \quad (10)$$

$$L = \sqrt{(x_a - x_b)^2 + (y_a - y_b)^2 + (z_a - z_b)^2} \quad (11)$$

where L is the length of the wall at a interest-region.

3 Case study

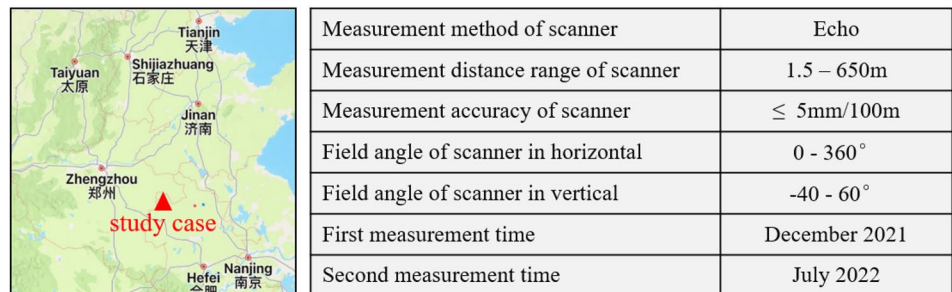
3.1 Overview and monitoring process

A case study was conducted in Jianglou Village, Bozhou City, China. Figure 5a shows the geographical location of the village. This village mainly consists of brick-concrete buildings, which get frequently damaged owing to perennial coal seam mining.

During the monitoring period, two measurements were performed at an interval of approximately seven months. The parameters and specifications of the TLS are shown in Fig. 5b, and the point cloud of the measured region is shown in Fig. 5c. In December 2021, the working face has not been mined below the buildings, which has little impact, so the first measurement was made. According to the mining plan, in January 2022, the mining of the working face has stopped, and the working face has been advanced to the building. After the mining stopped, the surface was still deformed. Therefore, after the deformation becomes stable, the second measurement was made in July 2022.

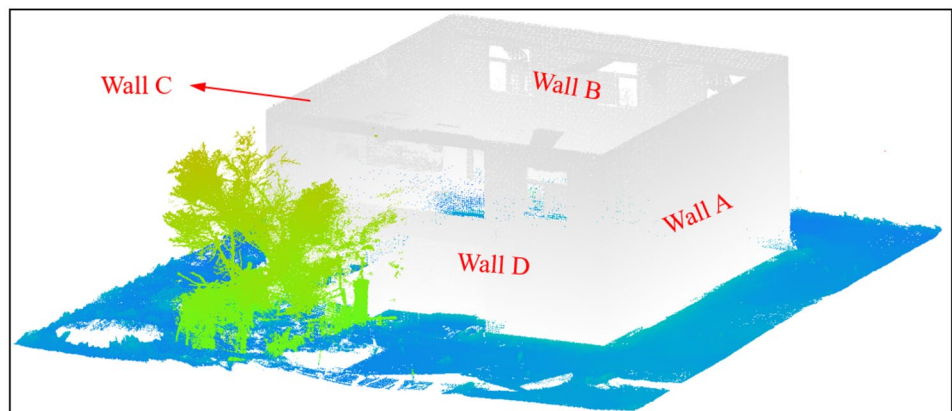
As show in in Fig. 6, after denoising, downsampling, and ground filtering the point cloud data, the point cloud sizes of first and second measurement are 2.6 and 3.5 points/cm² respectively. Then, we performed a building deformation analysis based on the length of the walls.

Fig. 5 Overview of the case study



(a) Location of the case study

(b) TLS parameters and measurement details



(c) Point cloud of the measured region in 3D space

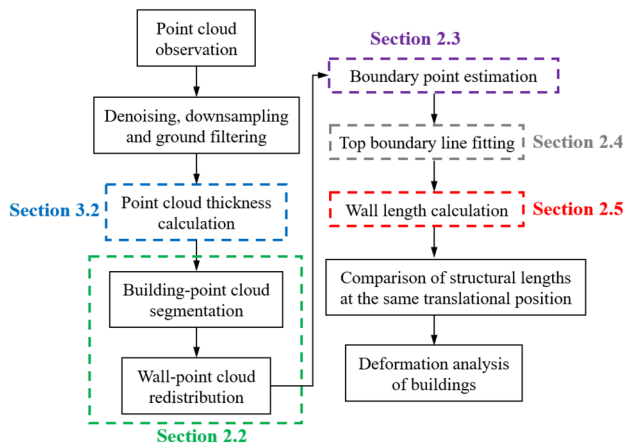


Fig. 6 Building deformation monitoring process

3.2 Calculation of wall-point cloud thickness

Assuming that a point cloud can be modeled by a plane, its thickness can be estimated using the distance between the points in the cloud and the plane. We randomly selected N points from the point cloud data of a single wall obtained from the first measurement and defined a neighborhood of radius R around each point to estimate the point cloud thickness of the walls.

Note that not all points in the neighborhood of a given point were retained. First, for every neighborhood, the distance between each point and the neighborhood plane was calculated. Next, considering the presence of noise, only those points were retained whose distance from the plane was less than the corresponding mean square distance. Thus, neighborhood-point cloud thickness can be obtained using Eq. (12). Subsequently, the wall-point cloud thickness was calculated, as shown by Eq. (13).

$$TH_{Nei} = \sum_{i=1}^n d_i/n, d_1 \leq d_2 \leq \dots \leq d_i \leq \dots \leq d_n \leq RMSE1 + d_{mean} = [\sum_{j=1}^m (d_j - d_{mean})^2/m] + d_{mean} \quad (12)$$

where $\mathbf{d} = [d_1, d_2, \dots, d_i, \dots, d_n]$ and $\mathbf{D} = [d_1, d_2, \dots, d_j, \dots, d_m]$ are the distance set between original and retained data points and the plane in a neighborhood, respectively; n and m are the number of points which in \mathbf{d} and \mathbf{D} , respectively; and d_{mean} is the mean distance in \mathbf{D} .

$$TH_{Wall} = \sum_{i=1}^N TH_{Nei}^i/M, TH_{Nei}^1 \leq TH_{Nei}^2 \leq \dots \leq TH_{Nei}^i \leq \dots \leq TH_{Nei}^N \leq RMSE2 + TH_{Nei}^{mean} = [\sum_{j=1}^M (TH_{Nei}^j - TH_{Nei}^{mean})^2/M] + TH_{Nei}^{mean} \quad (13)$$

where $\mathbf{th}_{Nei} = [TH\ 1\ Nei, TH\ 2\ Nei, \dots, TH\ j\ Nei, \dots, TH\ N\ Nei]$ and $\mathbf{TH}_{Nei} = [TH\ 1\ Nei, TH\ 2\ Nei, \dots, TH\ i\ Nei, \dots, TH\ M\ Nei]$ are the neighborhood-point cloud thickness set of original and retained neighborhoods, respectively; N and M

are the number of neighborhoods which in \mathbf{th}_{Nei} and \mathbf{TH}_{Nei} ; and $TH\ mean\ Nei$ is the mean neighborhood-point cloud thickness in \mathbf{TH}_{Nei} .

In this study, N was set to 40. The value of R was set to be in the range 5–20 cm and was increased in steps of 5 cm. Figures 7a–d show that the thickness of the neighborhood point clouds, and consequently, that of the wall-point cloud increase with R . However, for $R = 15$ cm, the change in the thickness of the point clouds was not noticeable. Therefore, we also performed the calculations for $R = 30$ and 40 cm.

Figures 7c–f show that for $R \geq 15$ cm, the thickness of the retained neighborhood point clouds did not change significantly and was approximately 3 cm. The thickness of the wall-point cloud calculated using the neighborhood point clouds also showed no significant change and was approximately 1.7 cm. Therefore, in this study, a wall-point cloud thickness of 1.7 cm corresponding to $N = 40$ and $R = 15$ cm was used as the benchmark to determine the distance threshold.

3.3 Deformation analysis based on wall length

As mentioned in Sect. 2.2, the distance thresholds for point cloud data segmentation and redistribution needs to be greater than or equal to the thickness of the wall-point cloud. Based on the results presented in Sect. 3.2, the distance thresholds for data segmentation and redistribution were determined to be 4.0 and 1.7 cm, respectively. The point cloud data of the building is shown in Fig. 8a. Because there were trees near wall D, the point cloud data of wall D (green point cloud) are missing in some areas. However, the point cloud data of the other walls were completely acquired.

Next, we estimated the boundary points of all the wall-point clouds. The outline of the building composed of the boundary points is shown in Fig. 8b. Owing to the measurement conditions, the boundary point data of wall D was slightly noisy; however, the inner and outer boundary points could be clearly distinguished, and hence, the subsequent analysis was not affected.

Subsequently, we fitted the top boundary line based on the top boundary points. We also calculated the intersection points of the boundary lines. Figure 8c shows that the intersection points are in perfect alignment with the vertical boundary lines. Thus, the fitted line is consistent with the actual data.

Finally, we calculated the lengths of all the walls. The height of the interest-region was considered to be $H = 0.25$ m, and the top boundary line was translated 20 times toward the bottom of the wall. The intersection points and length of the walls corresponding to each interest-region are shown in Fig. 8d and Table 1, respectively.

Information regarding the deformation of the building can be obtained by measuring the difference in the lengths

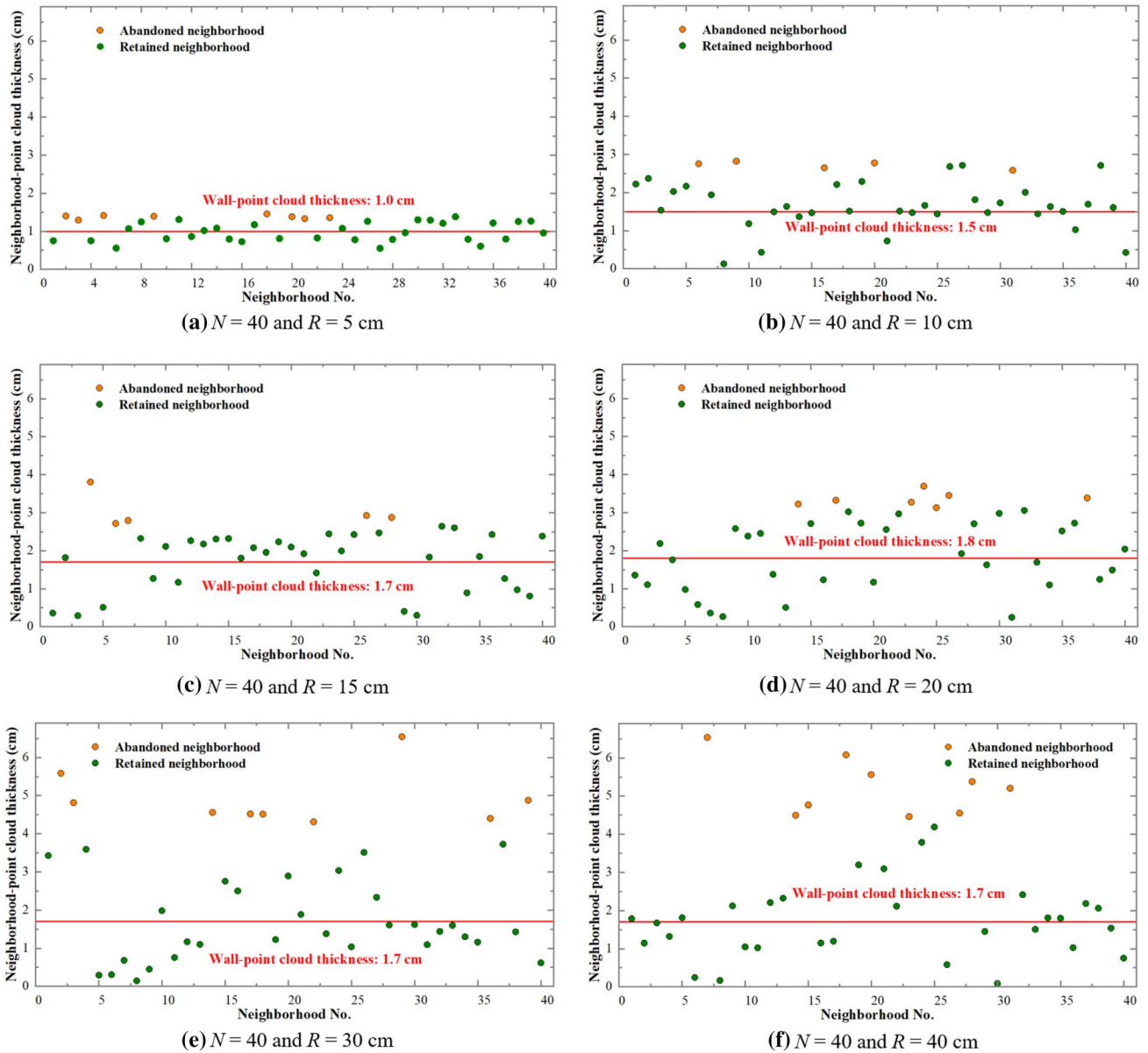


Fig. 7 Calculation results of wall-point cloud thickness

of the walls before and after deformation, as shown by Eq. (14). The results of the deformation analysis are shown in Fig. 9.

$$L_e = L_2 - L_1 \tag{14}$$

where L_e denotes the structural deformation of the walls, L_1 is the length of the wall measured at a particular position during the first measurement, and L_2 is the length of the wall measured at the same position during the second measurement.

From Table 1 and Fig. 9, we observe that the variation in the length of the walls with translation is quite similar

for the two measurements. The deformation of wall A was in the range 34–48 mm. If the 10th translation (i.e., the position 2.5 m below the roof) is considered to be the central reference point, then the deformation of wall A increased away from this point on both sides. Comparing these results with the photograph of wall A shown in Fig. 10a, we observe that the width of the crack on wall A gradually decreased from the roof toward the ground, but the number of cracks increased from one to two. Thus, the variation of the crack width is consistent with our deformation analysis. The deformation of wall B was small and in the range 0–12 mm. This is consistent with the fact that no cracks were observed on wall B during the

Fig. 8 Point cloud data at different steps of our calculation

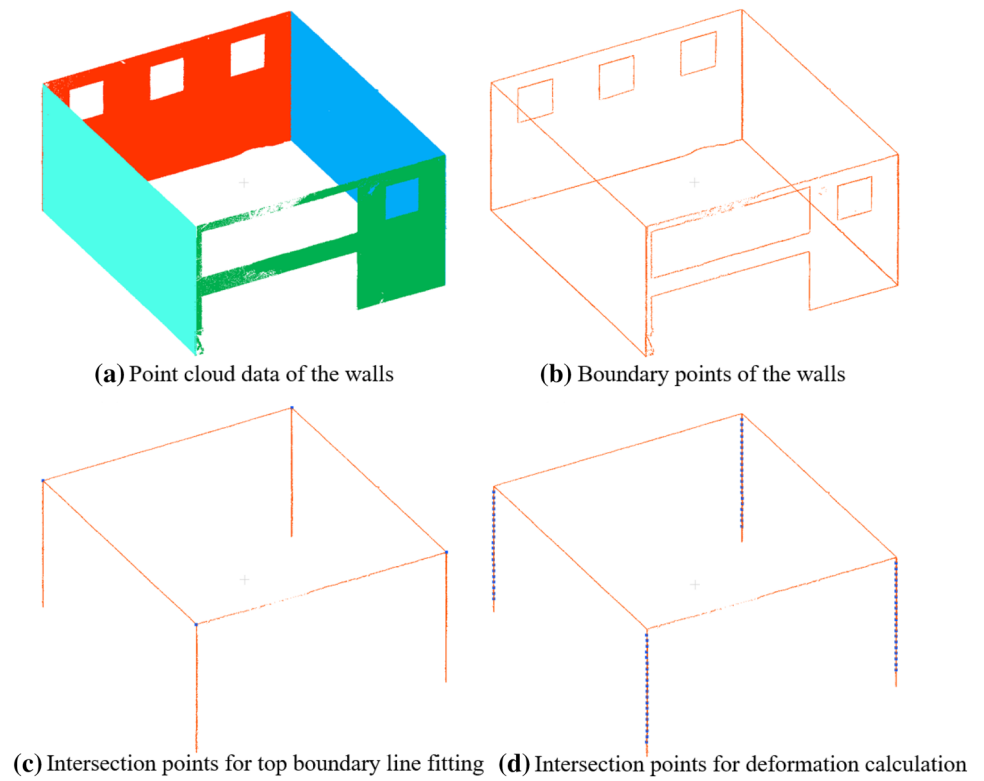


Table 1 Wall length before and after deformation

| No | Wall length from first measurement/mm | | | | Wall length from second measurement/mm | | | |
|----|---------------------------------------|--------|--------|--------|--|--------|--------|--------|
| | Wall A | Wall B | Wall C | Wall D | Wall A | Wall B | Wall C | Wall D |
| 1 | 12016 | 10791 | 11978 | 10825 | 12053 | 10792 | 11980 | 10856 |
| 2 | 12009 | 10795 | 11978 | 10825 | 12049 | 10796 | 11985 | 10857 |
| 3 | 12006 | 10795 | 11981 | 10824 | 12051 | 10803 | 11978 | 10858 |
| 4 | 12008 | 10793 | 11976 | 10824 | 12048 | 10803 | 11981 | 10857 |
| 5 | 12004 | 10790 | 11975 | 10822 | 12050 | 10799 | 11986 | 10849 |
| 6 | 12015 | 10790 | 11971 | 10819 | 12060 | 10796 | 11982 | 10842 |
| 7 | 12020 | 10790 | 11973 | 10810 | 12065 | 10797 | 11972 | 10844 |
| 8 | 12020 | 10786 | 11980 | 10813 | 12061 | 10799 | 11978 | 10845 |
| 9 | 12022 | 10785 | 11979 | 10812 | 12060 | 10797 | 11982 | 10840 |
| 10 | 12019 | 10790 | 11983 | 10815 | 12055 | 10796 | 11978 | 10838 |
| 11 | 12017 | 10793 | 11984 | 10807 | 12053 | 10795 | 11985 | 10839 |
| 12 | 12014 | 10795 | 11985 | 10809 | 12051 | 10797 | 11984 | 10839 |
| 13 | 12014 | 10791 | 11989 | 10811 | 12052 | 10797 | 11983 | 10833 |
| 14 | 12013 | 10787 | 11988 | 10808 | 12051 | 10795 | 11986 | 10833 |
| 15 | 12011 | 10787 | 11987 | 10804 | 12050 | 10795 | 11990 | 10831 |
| 16 | 12010 | 10784 | 11988 | 10805 | 12053 | 10795 | 11991 | 10829 |
| 17 | 12010 | 10783 | 11987 | 10807 | 12053 | 10795 | 11983 | 10830 |
| 18 | 12010 | 10785 | 11997 | 10810 | 12051 | 10795 | 11984 | 10838 |
| 19 | 12010 | 10785 | 11999 | 10813 | 12052 | 10794 | 11983 | 10842 |
| 20 | 12009 | 10782 | 11992 | 10812 | 12056 | 10793 | 11982 | 10836 |

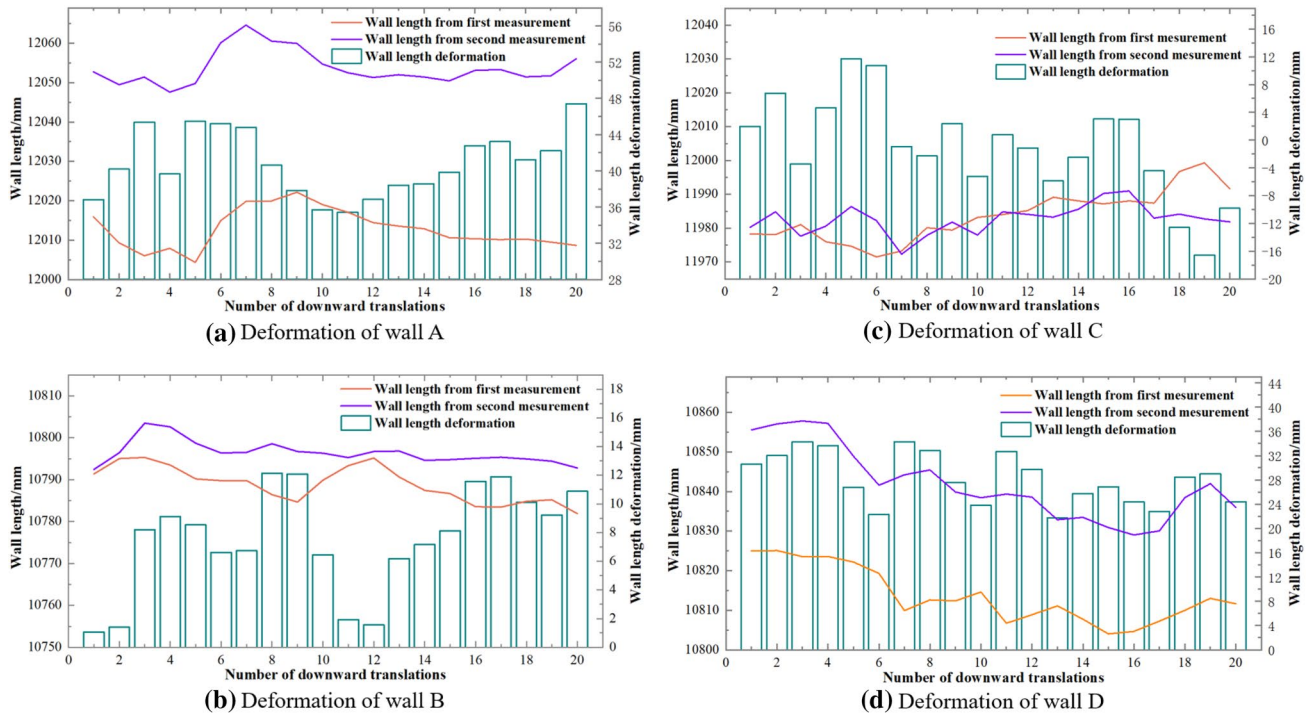
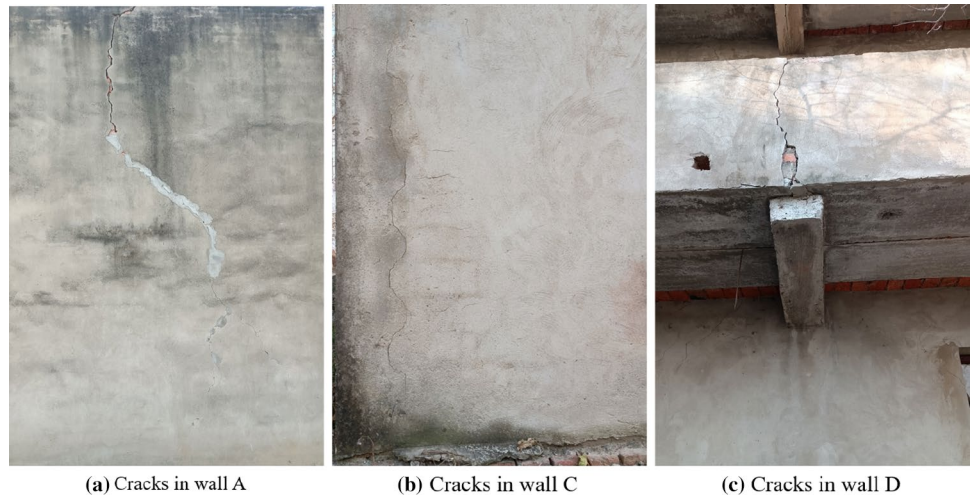


Fig. 9 Results of the deformation analysis based on the wall lengths

Fig. 10 Photographs of the walls



site investigation. The deformation of wall C was in the range – 18 to 12 mm, which was slightly larger than that of wall B. Only one fine crack was observed on wall C that extended from the top to the bottom of the wall, as shown in Fig. 10b. The deformation of wall D was in the range 0–36 mm. Comparing Figs. 5c and 10c, we observe that wall D contains the main sources of lighting for the building, namely, the doors and windows; consequently, cracks were observed on the non-wall areas of wall D. Note that the deformation of wall D did not fluctuate appreciably with translation, unlike that of wall A.

4 Discussion

4.1 Comparison of boundary point estimation methods

In Sect. 2.3, we introduced a few changes to the traditional boundary point estimation method based on normal vectors. In this section, we compare the method proposed in this study with the method based on normal vectors. The boundary point estimation time and the

corresponding results obtained using the point cloud data of the first measurement are shown in Table 2 and Fig. 11, respectively.

Table 2 shows that the method in this study is approximately 10 times faster than the method based on normal vectors. This is because the proposed method avoids recalculating the neighborhood normal vectors, and hence, does not need to re-estimate the coordinates of each neighborhood point cloud. It only calculates the neighborhood normal vectors once, and subsequently transforms the coordinate system once. As shown in Fig. 11, both the methods successfully estimated the boundary points of the walls. To further compare the boundary point estimation results, we calculated the absolute error introduced in the wall length at the same location for both the methods. The maximum error was approximately 8 mm, and the average error was in the range 0–5 mm, as shown in Fig. 12.

Our results confirm that although the boundary points estimated by both the methods are accurate, the estimation time of the method proposed in this study is significantly shorter than that of the method based on normal vectors.

Table 2 Boundary point estimation time

| Estimated using the method in this study | | | | |
|--|-----|-----|-----|------|
| Wall | A | B | C | D |
| Time/s | 525 | 486 | 418 | 1584 |
| Estimated using the method based on normal vectors | | | | |
| Wall | A | B | C | D |
| Time/h | 1.4 | 1.3 | 1.1 | 4.1 |

4.2 Effect of weight function on wall length

In addition to IGG, Huber and Hampel are also commonly used weighting function. Unlike the IGG weight function, which divides the data into three segments, the Huber weight function divides the data into two segments, as shown by Eq. (16); whereas, the Hampel weight function divides the data into four segments, as shown by Eq. (17). We calculated the wall lengths based on the boundary points obtained from the first measurement for these three weight functions. In addition, we compared the wall lengths calculated using the three weight functions and obtained the corresponding errors.

As shown in Fig. 13, the absolute error value between Huber and IGG for wall A was about 6 mm at one position. In the absolute error value between Hampel and IGG, that for wall B was about 7 mm at one position. The absolute errors at other positions were in the range 0–5 mm. This difference in the absolute errors is mainly owing to the different behaviors of the three weight functions. However, the weight function did not have a significant influence on the final results, and the error introduced by it was below 5 mm.

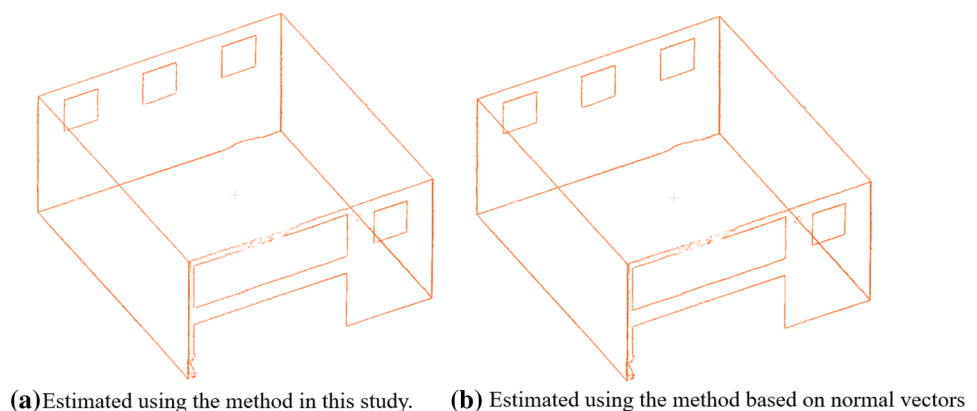
$$p_{ii} = \begin{cases} 1 & |v_i| < s\sigma_0 \\ s\sigma_0/|v_i| & |v_i| > s\sigma_0 \end{cases} \quad (16)$$

where s is the threshold coefficient to ensure robustness, which was set to 1.5 in this study.

$$p_{ii} = \begin{cases} 1 & |v_i| < s_1\sigma_0 \\ s_1\sigma_0/|v_i| & s_1\sigma_0 < |v_i| < s_2\sigma_0 \\ s_1(s_2\sigma_0 - |v_i|)/(s_1 - s_2)/|v_i| & s_2\sigma_0 < |v_i| < s_3\sigma_0 \\ 0 & |v_i| > s_3\sigma_0 \end{cases} \quad (17)$$

where s_1 , s_2 , and s_3 are the threshold coefficients used to ensure robustness, which were set to 1.5, 2.0, and 3.0, respectively.

Fig. 11 Comparison of boundary point estimation results



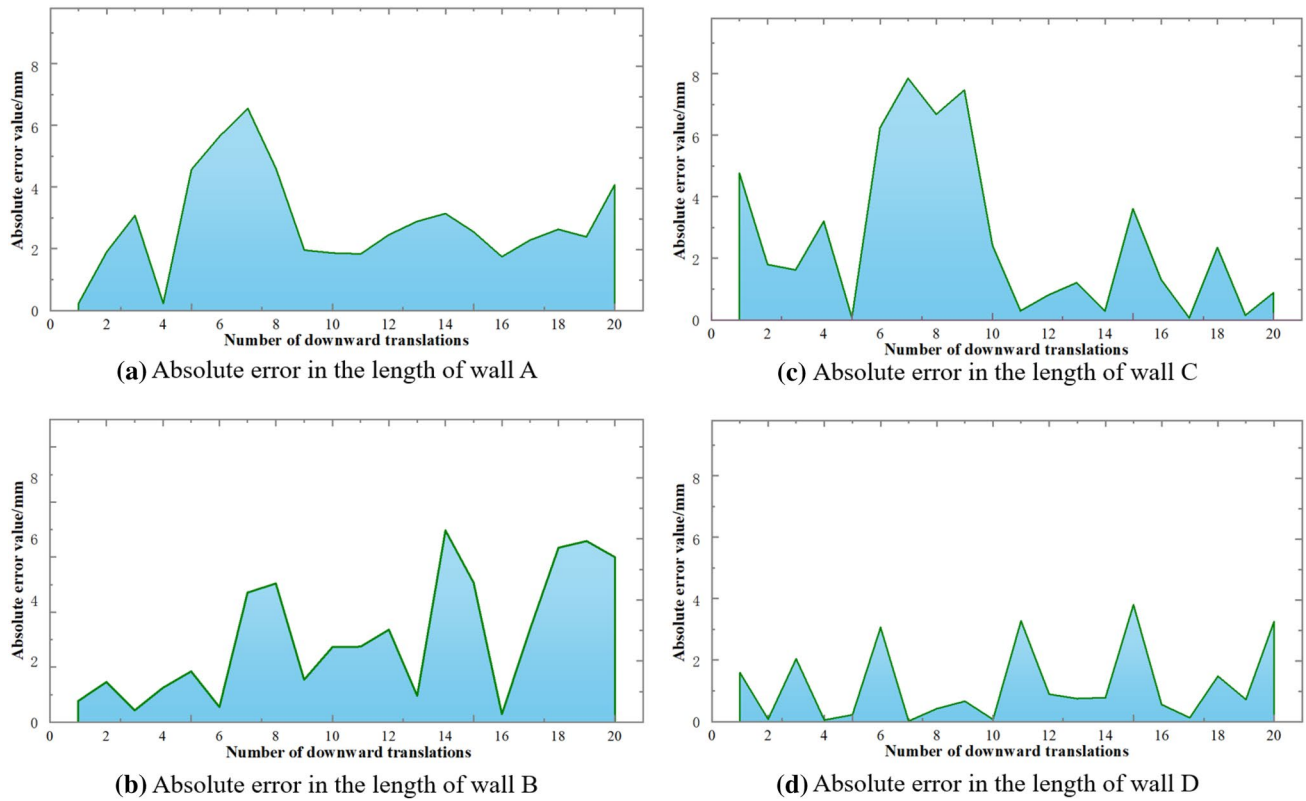


Fig. 12 Error in the wall length estimates introduced by the boundary point estimation method

4.3 Accuracy of wall length calculations

To determine the accuracy of our wall length calculations, we performed an additional measurement on wall A on the day of the second measurement. Considering distance thresholds of 4.0 and 1.7 cm and $H=0.25$ m, we calculated the length of wall A. Next, we calculated the ratio between the absolute value of the deformation and length of the wall (i.e., the deformation degree), as shown in Table 3.

The second and additional measurements were performed consecutively on the same day. Note that ideally the difference in the deformation values between these two measurements should be 0; therefore, the deformation values given in Table 3 can be regarded as the error and the deformation degree as the error rate for evaluating the accuracy of our calculations. The deformation values for the two consecutive measurements were in the range -6 to $+6$ mm. This arises mainly due to the measurement error of the TLS, registration error of the multi-station data, and other accidental errors. The deformation degree for the proposed method did not exceed $5/10000$; thus, our method exhibits good performance while achieving millimeter-level accuracy.

5 Conclusions

In this study, we proposed a wall length-based deformation monitoring method of brick-concrete buildings in mining area using terrestrial laser scanning. And the main conclusions are as follows. The deformation estimated using the proposed method was consistent with the actual deformation of the building as revealed by the wall cracks. The boundary point estimation method used in this study not only estimated the wall boundary points accurately but was also 10 times faster than the conventional method based on normal vectors. In the absence of any variable factors, the absolute error in the wall length did not exceed 8 mm and was mostly confined in the range 0–5 mm. In the WLS method, the weight function is a variable factor. Considering the IGG weight function as the reference, the absolute error in the wall lengths obtained using the Huber and Hampel weight functions was in the range of 0–5 mm. Keeping in mind that the difference in deformation between two consecutive measurements within a short interval of time should be ideally 0, the absolute error in the wall length obtained using the proposed method was in the range -6 to $+6$ mm. This confirms that our proposed method can achieve millimeter-level accuracy.

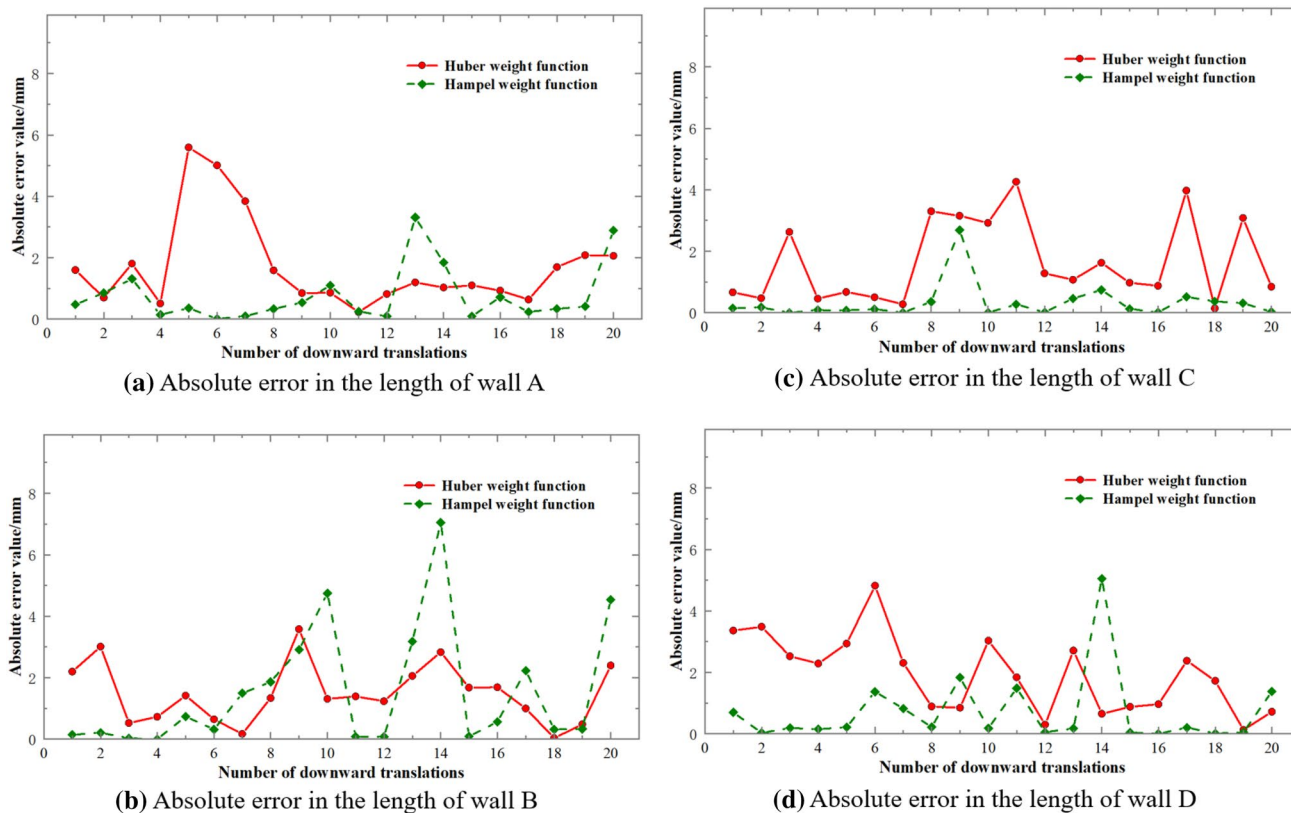


Fig. 13 Error in wall length measurement introduced by different weight functions

Table 3 Accuracy of the wall length calculations

| No | Wall length/mm | | Evaluating indicator | |
|----|-------------------|------------------------|----------------------|--------------------|
| | First measurement | Additional measurement | Deformation/mm | Deformation degree |
| 1 | 12053 | 12057 | 4 | 3/10000 |
| 2 | 12049 | 12055 | 6 | 5/10000 |
| 3 | 12051 | 12054 | 3 | 2/10000 |
| 4 | 12048 | 12054 | 6 | 5/10000 |
| 5 | 12050 | 12056 | 6 | 5/10000 |
| 6 | 12060 | 12057 | -3 | 2/10000 |
| 7 | 12065 | 12062 | -3 | 2/10000 |
| 8 | 12061 | 12064 | 3 | 3/10000 |
| 9 | 12060 | 12063 | 3 | 3/10000 |
| 10 | 12055 | 12060 | 5 | 4/10000 |
| 11 | 12053 | 12052 | 0 | 0/10000 |
| 12 | 12051 | 12050 | -2 | 1/10000 |
| 13 | 12052 | 12051 | -1 | 1/10000 |
| 14 | 12051 | 12056 | 5 | 4/10000 |
| 15 | 12050 | 12057 | 7 | 5/10000 |
| 16 | 12053 | 12058 | 4 | 4/10000 |
| 17 | 12053 | 12056 | 3 | 3/10000 |
| 18 | 12051 | 12054 | 3 | 2/10000 |
| 19 | 12052 | 12052 | 0 | 0/10000 |
| 20 | 12056 | 12053 | -3 | 2/10000 |

Acknowledgements The work was supported by the National Natural Science Foundation of China [Grant numbers 52074010, 41602357], and Anhui Science Fund for Distinguished Young Scholars [Grant numbers 2108085Y20].

Data availability The data presented in this study are available on request from the corresponding author.

Declarations

Conflict of interest The authors declare that they have no known competing financial interests or personal relationships that could have appeared to influence the work reported in this study.

References

- Albu-Jasim Q, Medina-Cetina Z, Muliana A (2022) Calibration of a concrete damage plasticity model used to simulate the material components of unreinforced masonry reinforced concrete infill frames. *Mater Struct* 55:36. <https://doi.org/10.1617/s11527-021-01845-0>
- Ren M, Cheng GW, Zhu WC, Nie W, Guan K, Yang TH (2021) A prediction model for surface deformation caused by underground mining based on spatio-temporal associations. *Geomat Nat Haz Risk* 13(1):94–122. <https://doi.org/10.1080/19475705.2021.2015460>
- Yue D, Wang D, Liu FY, Wang JJ (2022) A new data processing method for high-precision mining subsidence measurement using airborne LiDAR. *Front Earth Sci*. <https://doi.org/10.3389/feart.2022.858050>
- Jiang Q, Shi YE, Yan F, Zheng H, Kou YY, He BG (2021) Reconstitution method for tunnel spatiotemporal deformation based on 3D laser scanning technology and corresponding instability warning. *Eng Fail Anal*. <https://doi.org/10.1016/j.engfailanal.2021.105391>
- Wu SB, Zhang BC, Ding XL, Shahzad N, Zhang L, Lu Z (2022) A hybrid method for MT-InSAR phase unwrapping for deformation monitoring in urban areas. *J Appl Earth Observation Geoinform*. <https://doi.org/10.1016/j.jag.2022.102963>
- Xu NL, Huang DB, Song S, Ling X, Strasbaugh C, Yilmaz A, Sezen H, Qin RJ (2021) A volumetric change detection framework using UAV oblique photogrammetry—a case study of ultra-high-resolution monitoring of progressive building collapse. *Int J Digital Earth* 14(11):1705–1720. <https://doi.org/10.1080/17538947.2021.1966527>
- Hyungjoon S (2021) Tilt mapping for zigzag-shaped concrete panel in retaining structure using terrestrial laser scanning. *J Civil Struct Health Monit* 11:851–865. <https://doi.org/10.1007/s13349-021-00484-x>
- Tzortzinis G, Ai CB, Breña SF, Gerasimidis S (2022) Using 3D laser scanning for estimating the capacity of corroded steel bridge girders: experiments, computations and analytical solutions. *Eng Struct*. <https://doi.org/10.1016/j.engstruct.2022.114407>
- Nieto-Julián JE, Antón D, Moyano JJ (2019) Implementation and management of structural deformations into historic building information models. *Int J Archit Herit* 14:1384–1397. <https://doi.org/10.1080/15583058.2019.1610523>
- Rolin R, Antaluca E, Batoz JL, Lamarque F, Lejeune M (2019) From point cloud data to structural analysis through a geometrical hBIM-oriented model. *J Comput Cultural Herit* 12:1–26. <https://doi.org/10.1145/3242901>
- Lian XG, Dai HY, Ge LL, Cai YF (2020) Assessment of a house affected by ground movement using terrestrial laser scanning and numerical modeling. *Environ Earth Sci*. <https://doi.org/10.1007/s12665-020-08929-0>
- Batur M, Yilmaz O, Ozener H (2020) A case study of deformation measurements of istanbul land walls via terrestrial laser scanning. *IEEE J Sel Top Appl Earth Observations Remote Sens* 13:6362–6371. <https://doi.org/10.1109/JSTARS.2020.3031675>
- Li JY, Wang L (2021) Mining subsidence monitoring model based on BPM-EKTF and TLS and its application in building mining damage assessment. *Environ Earth Sci*. <https://doi.org/10.1007/s12665-021-09704-5>
- Yang F, Wen XT, Wang XS, Li X, Li ZQ (2021) A model study of building seismic damage information extraction and analysis on ground-based LiDAR data. *Adv Civil Eng* 2021:1–14. <https://doi.org/10.1155/2021/5542012>
- Matwij W, Gruszczynski W, Puniach E, Cwiakala P (2021) Determination of underground mining-induced displacement field using multi-temporal TLS point cloud registration. *Measurement*. <https://doi.org/10.1016/j.measurement.2021.109482>
- Zhou JX, Li F, Wang JA, Gao AQ, He CY (2022) Stability control of slopes in open-pit mines and resilience methods for disaster prevention in urban areas: a case study of Fushun west open pit mine. *Front Earth Sci*. <https://doi.org/10.3389/feart.2022.879387>
- Sun WX, Wang J, Jin FX (2020) An automatic coordinate unification method of multitemporal point clouds based on virtual reference datum detection. *IEEE J Sel Top Appl Earth Observations Remote Sens* 13:3942–3950. <https://doi.org/10.1109/JSTARS.2020.3008492>
- Varbla S, Ellmann A, Puust R (2021) Centimetre-range deformations of built environment revealed by drone-based photogrammetry. *Autom Constr*. <https://doi.org/10.1016/j.autcon.2021.103787>
- Sun Y, Wu F (2022) DESAC: differential evolution sample consensus algorithm for image registration. *Appl Intell*. <https://doi.org/10.1007/s10489-022-03266-0>
- Wang TR, Liu N, Yuan L, Wang KX, Sheng XJ, Dulikravich GS (2022) Iterative least square optimization for the weights of NURBS curve. *Math Probl Eng* 2022:1–12. <https://doi.org/10.1155/2022/5690564>
- Caboussat A, Glowinski R, Gourzoulidis D (2022) A least-squares method for the solution of the non-smooth prescribed Jacobian equation. *J Sci Comput* 93:15. <https://doi.org/10.1007/s10915-022-01968-8>
- Gong X, Li Z (2016) A robust weighted total least-squares solution with Lagrange multipliers. *Surv Rev* 49:176–185. <https://doi.org/10.1080/00396265.2016.1150088>
- Sun WX, Wang J, Jin FX, Li YY, Yuan YK (2022) An adaptive cross-section extraction algorithm for deformation analysis. *Tunn Undergr Space Technol* 121:0886–7798. <https://doi.org/10.1016/j.tust.2021.104332>

Publisher's Note Springer Nature remains neutral with regard to jurisdictional claims in published maps and institutional affiliations.

Springer Nature or its licensor (e.g. a society or other partner) holds exclusive rights to this article under a publishing agreement with the author(s) or other rightsholder(s); author self-archiving of the accepted manuscript version of this article is solely governed by the terms of such publishing agreement and applicable law.